OXFORD

Cerebral Cortex, 2015, 1–16

doi: 10.1093/cercor/bhv124
Original Article

ORIGINAL ARTICLE

Selective Thalamic Innervation of Rat Frontal Cortical Neurons

Naoki Shigematsu[1,2,3], Yoshifumi Ueta[1,3], Alsayed A. Mohamed[1,4], Sayuri Hatada[1], Takaichi Fukuda[2], Yoshiyuki Kubota[1,3,5], and Yasuo Kawaguchi[1,3,5]

[1]Division of Cerebral Circuitry, National Institute for Physiological Sciences, Okazaki 444-8787, Japan, [2]Department of Anatomy and Neurobiology, Graduate School of Medical Sciences, Kumamoto University, Kumamoto 860-8556, Japan, [3]JST, CREST, Tokyo 102-0076, Japan, [4]Department of Anatomy and Embryology, Faculty of Veterinary Medicine, South Valley University, Qena 83523, Arab Republic of Egypt and [5]Department of Physiological Sciences, SOKENDAI (Graduate University for Advanced Studies), Okazaki 444-8787, Japan

Address correspondence to Prof. Yasuo Kawaguchi, Division of Cerebral Circuitry, National Institute for Physiological Sciences, Okazaki 444-8787, Japan. Email: yasuo@nips.ac.jp

Abstract

Most glutamatergic inputs in the neocortex originate from the thalamus or neocortical pyramidal cells. To test whether thalamocortical afferents selectively innervate specific cortical cell subtypes and surface domains, we investigated the distribution patterns of thalamocortical and corticocortical excitatory synaptic inputs in identified postsynaptic cortical cell subtypes using intracellular and immunohistochemical staining combined with confocal laser scanning and electron microscopic observations in 2 thalamorecipient sublayers, lower layer 2/3 (L2/3b) and lower layer 5 (L5b) of rat frontal cortex. The dendrites of GABAergic parvalbumin (PV) cells preferentially received corticocortical inputs in both sublayers. The somata of L2/3b PV cells received thalamic inputs in similar proportions to the basal dendritic spines of L2/3b pyramidal cells, whereas L5b PV somata were mostly innervated by cortical inputs. The basal dendrites of L2/3b pyramidal and L5b corticopontine pyramidal cells received cortical and thalamic glutamatergic inputs in proportion to their local abundance, whereas crossed-corticostriatal pyramidal cells in L5b exhibited a preference for thalamic inputs, particularly in their distal dendrites. Our data demonstrate an exquisite selectivity among thalamocortical afferents in which synaptic connectivity is dependent on the postsynaptic neuron subtype, cortical sublayer, and cell surface domain.

Key words: corticocortical cell, corticopontine cell, corticostriatal cell, parvalbumin cell, thalamocortical input

Introduction

The thalamus not only relays information about peripheral sensations to primary sensory areas, but also motor information from the basal ganglia and cerebellum to frontal cortical areas (Jones 2007; Strick et al. 2009). In the rat somatosensory cortex, layer 4 (L4) receives dense thalamic inputs (Jones 2009), with lower L5 (L5b) cells also receiving direct thalamic inputs (Constantinople and Bruno 2013). On the other hand, in the rodent frontal cortex, which lacks a cytoarchitectonically defined layer 4, thalamocortical input is most prominent in the lower part of L2/3 (L2/3b), but is also present in both L5b and layer 1 (L1) (Kuramoto et al. 2009; Rubio-Garrido et al. 2009; Morishima et al. 2011). Although thalamic innervation patterns have been well analyzed in the sensory cortex, especially in L4 cells, it remains to be investigated in the frontal areas (White and Rock 1980; Benshalom and White 1986; Peters and Payne 1993;

Richardson et al. 2009; da Costa and Martin 2011; Schoonover et al. 2014). Comparative analysis of thalamocortical synapse formation between sensory and frontal areas will be critical for understanding the functional roles of thalamic inputs to these different cortical areas.

Neocortical neurons are composed of glutamatergic pyramidal and GABAergic nonpyramidal cells. Pyramidal cells receive excitatory inputs mainly at dendritic spines (DeFelipe and Fariñas 1992). On the other hand, excitatory inputs to GABAergic cells typically occur on smooth dendritic shafts and somatic surfaces (Gulyás et al. 1999). Furthermore, proximal and distal dendrites integrate excitatory input in different ways (Nörenberg et al. 2010; Branco and Häusser 2011). Therefore, to understand the function of cortical circuits, we need to determine whether excitatory synaptogenesis is specialized based on postsynaptic neuron type (pyramidal cells, GABAergic cells, or their subtypes), on neuronal surface type (dendritic spines, dendritic shafts, and/or somata), or on dendritic locations (proximal or distal portions) (Stepanyants et al. 2004; Yuste and Bonhoeffer 2004). A key question is whether thalamocortical synapses are formed purely according to the relative local abundance of thalamocortical fibers, or if thalamic inputs preferentially innervate specific postsynaptic target domains.

In L4 of the somatosensory cortex, spiny stellate cells that receive thalamic inputs project forward to layer 2/3 (L2/3) pyramidal cells that, in turn, innervate pyramidal neurons in layer 5 (L5). In the rat frontal cortex, L2/3b pyramidal cells are mostly corticocortical cells (Ueta et al. 2013, 2014). On the other hand, L5b cells project not only to cortical areas but also to subcortical structures. The major L5b subcortical projection subtypes are corticopontine (CPn) and crossed-corticostriatal (CCS) cells (Morishima and Kawaguchi 2006; Otsuka and Kawaguchi 2008; Morishima et al. 2011), each of which exhibits distinct physiological, morphological, and connectional characteristics (Morishima et al. 2011; Avesar and Gulledge 2012). L2/3b pyramidal cells innervate both CPn and CCS cells in L5b (Otsuka and Kawaguchi 2008). However, the innervation patterns of thalamic fibers in the frontal cortex have not been investigated in either L2/3b or L5b pyramidal cells. Similarly, little is known about selective thalamic innervation of cortical parvalbumin (PV)-expressing cells, which comprise a major subtype of GABAergic cell in the cortex (Uematsu et al. 2008) and participate in thalamocortical feedforward inhibition (Agmon and Connors 1992; Gibson et al. 1999).

The aim of this study was to test whether cortical cells exhibit selective innervation from thalamocortical and corticocortical afferents according to neuron subtype and/or cell surface domain, or whether excitatory inputs are instead stochastically distributed on cortical cells based on the local spatial overlap of axons and dendrites. In order to evaluate the sources of inputs to specific cell subtypes and the locations of those inputs on the dendritic arbors, we used a combination of postsynaptic cell filling and presynaptic axon labeling in L2/3b and L5b of the rat secondary motor area (M2, Ueta et al. 2014). Cell subtypes that were filled with Lucifer yellow (LY) were identified either by retrograde labeling or by agglutinin labeling. Input sources were labeled by antibody staining with the vesicular glutamate transporter type 1 (VGluT1) or type 2 (VGluT2) to distinguish corticocortical and thalamocortical inputs, respectively (Fujiyama et al. 2001; Graziano et al. 2008). Putative synapses were identified by apposition of presynaptic label to postsynaptic cells observed with confocal laser scanning microscopy (CLSM) and validated by electron microscopic (EM) reconstructions. We quantified the ratios of VGluT2 inputs among total glutamatergic inputs within cortical sublayers overall, and compared these with the ratios on various postsynaptic somatic and dendritic domains for each cell subtype. Our results reveal that glutamatergic input densities and thalamic input ratios are highly correlated with neuron subtype, surface domain, and thalamorecipient sublayer in the rat frontal cortex.

Materials and Methods

Animals

Male Wistar rats were used in accordance with the guidelines of the Animal Care and Use Committee of the National Institute for Physiological Sciences and Kumamoto University.

Retrograde Tracer Labeling by Focal Iontophoretic Injections into the Frontal Cortex

Following are retrograde tracers used: 1) Alexa Fluor 555-conjugated cholera toxin subunit B (CTB555, Life Technologies Corporation, Grand Island, NY, USA), 2) Fast Blue (Dr Illing GmbH and Co. KG, Groß-Umstadt, Hesse, Germany), and 3) Diamidino Yellow (Dr Illing GmbH and Co. KG). CTB555 could be deposited in restricted layers by iontophoresis, used for laminar innervation analysis (Hirai et al. 2012; Ueta et al. 2014), as well as in most layers by pressure application, used for distribution analysis of projection cells. Fast Blue, which labels the cytoplasm, and Diamidino Yellow, which labels the nucleus, were used for intracellular injection of LY (Sigma-Aldrich Co. LLC, St Louis, MO, USA) into pyramidal cells of projection identification.

Animals (6–7 weeks old) were anesthetized with a mixture of ketamine (40 mg/kg, intraperitoneal [i.p.]) and xylazine (4 mg/kg, i.p.) and then injected with glycerol (0.6 g/kg, i.p.) and dexamethasone (1 mg/kg, intramuscular [i.m.]) before being placed in a stereotaxic apparatus. The CTB555 (0.2% in distilled water) was applied to the M2 area (4.5 mm anterior to the bregma, 1.5 or 1.7 mm lateral to the midline, inclined anteriorly by 25°; Ueta et al. 2014) through iontophoresis (negative current, 0.3 μA; 7-s on/off cycles; 20 min) with glass pipettes (tip diameter, 20–30 μm) backfilled with 0.9% NaCl. For retrogradely labeling of thalamocortical cells innervating whole cortical depth of M2, CTB555 was injected from L1 to upper L6 by pressure (PV820, World Precision Instruments, Inc., Sarasota, FL, USA) through glass pipettes (tip diameter, 50–100 μm). After a survival period of 4–6 days, the animals were deeply anesthetized with sodium pentobarbital (60 mg/kg, i.p.) and transcardially perfused with a prefixative (0.02 M phosphate buffer [PB] solution containing 8.56% sucrose and 5 mM $MgCl_2$), followed by a fixative (4% paraformaldehyde and 0.2% picric acid in 0.1 M PB). The animals were postfixed for 2 h at room temperature. Using a vibrating microtome (Leica Microsystems, Inc., Buffalo Grove, IL, USA), the brain ipsilateral to the tracer injection was sagittally cut into 20-μm sections. Every serial section ranging from around 0.6–3 mm from the midline, including almost all the parts of the ventral anterior/ventromedial (VA/VM) and ventrolateral (VL) thalamic nuclei, were collected. For observing the tracer deposits in M2, every other section was incubated overnight at 4°C with a mouse monoclonal antibody against the neurofilament heavy chain (N200 antibody, N0142, Sigma-Aldrich Co. LLC; 1:1000; to identify M2 area; Ueta et al. 2014) and a guinea pig polyclonal antibody against VGluT2 (AB2251, EMD Millipore Corporation, Billerica, MA, USA; 1:2000) in 0.05 M Tris-buffered saline (TBS) containing 10% normal goat serum, 2% bovine serum albumin (BSA), and 0.2% Triton-X-100 (Triton-X). After washing in TBS,

the sections were reacted with secondary antibodies that were conjugated to Alexa Fluor 350 (for N200; Life Technologies Corporation; 1:200) and Alexa Fluor 488 (for VGluT2; Life Technologies Corporation; 1:200) for 2–3 h at room temperature. For observing labeled thalamic cells, every adjacent section was incubated at 4°C with a mouse monoclonal antibody against neuronal nuclei (NeuN; MAB377, EMD Millipore Corporation; 1:5000) and a rabbit polyclonal antibody against calbindin D-28K (CB-38a, Swant, Marly, Switzerland; 1:2000). After washing in TBS, the sections were reacted with secondary antibodies conjugated to Alexa Fluor 350 (for NeuN) and Alexa Fluor 488 (for calbindin). The sections were mounted in SlowFade gold antifade reagent (Life Technologies Corporation).

Simultaneous Immunofluorescence for PV and VGluTs

Under deep anesthesia with sodium pentobarbital (70 mg/kg, i.p.), the animals (7–8 weeks old) were perfused with the prefixative, which was followed by 4% paraformaldehyde containing 0.2% picric acid and 0.1% glutaraldehyde in 0.1 M PB. The animals were left for 2 h at room temperature for postfixation. Oblique horizontal sections containing M2 (50-µm thickness; Kawaguchi et al. 1989) were cut using a vibrating microtome.

After incubation in PB containing 15% sucrose for 1 h and 30% sucrose for 2 h, the sections were subjected to freezing in liquid N_2 and thawing and then incubated with a mouse monoclonal antibody against PV (235, Swant; 1:5000), a rabbit polyclonal antibody against the VGluT1 (a generous gift from Dr T. Kaneko, Kyoto University, Kyoto, Japan; 1:100), and a guinea pig polyclonal antibody against VGluT2 (a generous gift from Dr T. Kaneko; 1:100) in TBS containing 1% BSA, 0.5% Triton-X, and 0.1% sodium azide for 7 days at 4°C. After several rinses in PB, the sections were incubated with a biotinylated anti-rabbit IgG (Vector Laboratories, Inc., Burlingame, CA, USA; 1:200) overnight and then further incubated with a mixture of streptavidin-conjugated Cy5 (Jackson ImmunoResearch, West Grove, PA, USA; 1:200), fluorescein isothiocyanate (FITC)-conjugated anti-mouse IgG (EMD Millipore Corporation; 1:100), and Cy3-conjugated anti-guinea pig IgG (EMD Millipore Corporation; 1:100) overnight.

Notably, previous studies have shown the colocalization of VGluT1 and VGluT2 immunoreactivities in the mouse brain (Graziano et al. 2008). However, we used rat brain tissues as the experimental materials, and the antibodies against VGluTs that we used for this study specifically reacted with each antigen protein without nonspecific immunoreaction. Thus, we rarely detected the colocalization of VGluT1/T2 immunolabeling in the following observations using a CLSM.

We investigated the tissue permeability of the primary antibodies from the section surface using CLSM. The antibodies against PV and VGluT2 penetrated along the whole depth of the sections. However, immunopositive reactions to the anti-VGluT1 antibody were found only within 5 µm of the surface. Thus, simultaneous observation of VGluT-positive bouton appositions was limited to within 5 µm of the section surface.

Intracellular Staining of Identified Cells after Fixation

Retrograde Labeling of Pyramidal Cells

The animals were anesthetized with ketamine (40 mg/kg, i.m.) and xylazine (4 mg/kg, i.m.). Stereotaxic injections of Fast Blue (7% in distilled water) and Diamidino Yellow (2% in distilled water) were made with coordinates derived from the Rat Brain Atlas (Paxinos and Watson 2007). Tracers were injected into the ipsilateral pons (7.2 mm posterior to the bregma, 1.5 mm lateral to the midline; depth, 9.0–9.8 mm) and the contralateral striatum through glass pipettes by pressure application for identifying CPn and CCS cells, respectively, in L5b. For contralateral striatum injection, the skull was partially uncovered, and the cerebral cortex, hippocampus, and fimbria just caudal to the striatum were removed by aspiration, and then the tracer was obliquely applied through the lateral ventricle (3 mm lateral from the midline at 4–5 mm depth while tilted 52–55° caudally). For labeling L2/3b pyramidal cells, the tracers were injected into the ipsilateral primary motor area (anteroposteriorly at the bregma, 2.0 mm lateral to the midline; depth, 0.7–0.8 mm) and contralateral M2. For M2 injection, a glass micropipette was obliquely set to apply the tracer at the same angle as the apical main shafts of M2 pyramidal cells.

Animal Fixation

Rats without or with tracer injections (3–5 days after the injection) were perfused with 4% paraformaldehyde in 0.1 M PB and postfixed for 30 min. Oblique horizontal sections of 300-µm thickness were cut using a vibrating microtome.

PV Cell Identification by Fluorescent Agglutinin Labeling

Sections were incubated with 0.1 M PB containing 40 µg/mL FITC-conjugated *Vicia villosa* agglutinin (VVA: Vector Laboratories, Inc.) (Ojima 1993). Almost all VVA-labeled neurons were positive for PV (Kubota et al. 2011a).

LY Injection

Sections were placed in a chamber filled with PB that was on the stage of a fluorescence microscope (Leica DM-LFS microscope, Leica Microsystems, Inc.). Under direct observation, the cell bodies labeled with FITC-conjugated VVA or fluorescent retrograde tracers (Fast Blue or Diamidino Yellow) were penetrated with a sharp glass pipette filled with LY (8% in 0.05 M Tris–HCl buffer; electrode resistance, 100–120 MΩ) and stained by an application of negative currents (7–10 nA, 2 min; voltage-clamp mode of a multiclamp 700B amplifier, Molecular Devices, LLC, Sunnyvale, CA, USA).

VGluT Immunofluorescence Applied to LY-Injected Cells

Slices containing neurons filled with LY were again fixed in 4% paraformaldehyde, 0.1% glutaraldehyde, and 0.2% picric acid in 0.1 M PB overnight and resectioned at a 25- or 50-µm thickness. After immunostaining for VGluTs with the above-mentioned procedure, the sections were mounted in Vectashield (Vector Laboratories, Inc.).

CLSM Observations

Sections were examined using CLSM (Fluoview FV1000, Olympus Corporation, Tokyo, Japan/Nikon D-ECLIPSE C1, Nikon Corporation, Tokyo, Japan). Using high-resolution CLSM, images were obtained with a 60× or 100× oil-immersion objective (numerical aperture = 1.4) and a 2× zoom factor. Single laser beams (473, 559, and 635 nm wavelengths) were alternately used to collect images of the different fluorescent signals. The somata and dendritic arborizations of LY-filled neurons were reconstructed by Autoneuron and the image stack module of the Neurolucida System (MBF Bioscience, Williston, VT, USA).

EM Observations of the Bouton Appositions Observed Using CLSM

For observations using a transmission EM (TEM; Hitachi H-7500, Hitachi High-Technologies Corporation, Tokyo, Japan) that were

made after using CLSM, the sections were incubated in TBS containing 1% BSA and 0.1% sodium azide with a mixture of an antibody against PV (mouse monoclonal antibody, Swant; 1:5000) or against LY (biotin-XX-conjugated rabbit anti-LY, A-5751, Life Technologies Corporation; 1:500) and an antibody against either of VGluTs (generous gifts from Dr T. Kaneko, guinea pig polyclonal antibodies; 1:100 each) at 4°C for 3 days. Following this, the sections were incubated with a Nanogold-conjugated anti-guinea pig IgG (Nanoprobes, Yaphank, NY, USA; 1:100) alone or a mixture with a biotinylated anti-mouse (Vector Laboratories, Inc.; 1:200) overnight. VGluT1 or VGluT2 immunoreactivity was visualized with silver enhancement using the HQ Silver Enhancement Kit (Nanoprobes) and then treated with a standard avidin–biotin–peroxidase complex (Vector Laboratories, Inc.; 1:100) for 2 h at room temperature. After color development with 3,3′-diaminobenzidine tetrahydrochloride (DAB) for visualizing PV or LY, the sections were postfixed with 1% OsO_4 for 15 min on ice, stained en bloc with uranyl acetate, dehydrated, and embedded in Araldite. Serial ultrathin sections of 65–70 nm in thickness were cut from the superficial part of the re-embedded specimens, lightly stained with uranyl acetate and lead citrate, and examined using TEM.

For diamond-knife serial block-face scanning EM (SBEM; 3View-Merlin, Gatan, Inc., Pleasanton, CA, USA, and Carl Zeiss AG, Oberkochen, Germany) observations made after using CLSM, the sections were incubated in TBS containing 1% BSA and 0.1% sodium azide with a biotin-XX-conjugated antibody against LY (Life Technologies Corporation; 1:2000) at 4°C for 3 days. Following this, the sections were incubated with the standard avidin–biotin–peroxidase complex (1:100) for 3 h at room temperature. After color development with nickel DAB for visualizing LY, light micrographs of LY-stained neurons were captured. Then, the sections containing the dendritic segments were processed using the modified heavy metal staining protocol (Wilke et al. 2013). In brief, the sections were postfixed with 2% OsO_4 and 1.5% potassium ferrocyanide in 0.1 M PB for 1 h on ice, which was followed by incubation with a 1% thiocarbohydrazide solution for 20 min at room temperature. Following this, the sections were again postfixed with 2% OsO_4 in 0.1 M PB for 30 min at room temperature and stained en bloc with 1% uranyl acetate at 4°C overnight. The sections were then incubated in Walton's lead aspartate solution at 60°C for 30 min, dehydrated, and embedded in Durcupan ACM resin (Sigma-Aldrich Co. LLC). The resin block containing the LY-stained dendritic segments was glued to the rivets with silver epoxy (SPI Supplies, West Chester, PA, USA). The entire block surface was covered by the silver paste (PELCO Conductive Silver Paint, Ted Pella, Inc., Redding, CA, USA) to avoid charging the resin. The mounted block was transferred to a chamber of SBEM, and serial ultrathin sections of 60 nm in thickness were cut from the block surface of the specimen. The freshly exposed surface of the block was imaged at 2-kV accelerating voltage and 60-pA beam current (cross-over mode) using the Gatan detector with 0.5 µs dwell time/pixel, 3.1 nm pixel size, and 16 k × 16 k image size. With contrast inversion, TEM-like contrast and comparable imaging information were achieved. A large volume dataset, including the entire dendritic segment, was serially acquired after cutting the block surface with a 60-nm-thick slice of 240 serial section images. The cubic size of the volume was 50 × 50 × 15 µm. The serial image alignment was done using homemade scripts for MATLAB (The MathWorks, Inc., Natick, MA, USA), kindly offered by Dr S. Mikula at The Max Planck Institute, Heidelberg, Germany. The dendritic and synaptic structures were rendered using 3D reconstruction software, Reconstruct (http://synapses.clm.utexas.edu/tools/index.stm; Fiala 2005).

Data Analysis

Appositions of the VGluT-immunolabeled boutons were observed and quantitatively analyzed using imaging software associated with the microscope (FV10-ASW 2.0 Viewer [Olympus Corporation] and EZ C1 viewer 340 [Nikon Corporation]). Z-stack images of the serial fluorescent sections and modifications of EM images were made using ImageJ 1.44 (NIH; http://imagej.nih.gov/ij/) and Adobe Photoshop CS5 software (Adobe Systems, Inc., San Jose, CA, USA). As shown in previous study, LY injection to pyramidal cells in fixed-slice has a drawback that apical dendrites are not fully visualized, especially those of L5b pyramidal cells (Matsubara et al. 1996). In L2/3b pyramidal cells, the apical dendritic tufts were not stained, but oblique dendrites were labeled. So we excluded the observation of bouton appositions on all apical dendrites in L5b pyramidal cells and apical tufts in L2/3b pyramidal cells from the present study. We estimated the proportion of VGluT2-labeled boutons among total VGluT-labeled boutons in the local space (spatial T_2 ratio), by counting VGluT1- and T2-positive boutons in randomly selected rectangular cubes in L2/3b and in L5b.

Statistical examinations were performed using StatView 5.0 software (SAS Institute, Inc., Cary, NC, USA) and GraphPad Prism 6.0 software (GraphPad Software, San Diego, CA, USA). The data are presented as the mean ± standard deviation (SD). Significance was set at P values of <0.05.

To obtain the total number of bouton appositions on PV cell somata, we first calculated the surface density of appositions from the area and apposition number of the partial somatic surface. Assuming the prolate spheroid shapes of the PV cell somata, the whole surface area of the PV cell somata was deduced from the maximum radius (Max) and the minimum radius (Min) of the reconstructed PV cell somata as follows:

$$2\pi\left\{(\mathrm{Min})^2+(\mathrm{Max})^2\times\frac{Æ}{\tan(Æ)}\right\},\ Æ=\arccos\left(\frac{\mathrm{Min}}{\mathrm{Max}}\right)$$

We estimated the total apposition number by multiplying the density by the total surface area.

Results

Thalamic Origins of Inputs to L2/3b and L5b of the Rat Frontal Cortex

In the M2 area, thalamocortical fiber density is heterogeneous across cortical depth, as shown by the uneven expression of VGluT2 that is present at higher densities in upper L1 (L1a), L2/3b, and L5b of frontal cortex (Fig. 1*B*; Morishima et al. 2011). M2 is innervated by thalamic nuclei including VA/VM nuclei and the VL nucleus. Calbindin-positive cells are more abundant in VA/VM nuclei than in VL nucleus (Fig. 1*C*,*D*; Ushimaru et al. 2012). When the retrograde tracer CTB555 was injected extensively from L1 to L5 in M2 by pressure, 81.8% of the labeled thalamic cells were in the VA/VM nuclei, whereas 18.3% were in the VL nucleus (Fig. 1*A*,*C*; whole-depth injection; 5040 thalamic cells from 2 rats). Therefore, VA/VM neurons innervated M2 more than did neurons in VL.

Next, we identified the thalamic cells innervating L2/3b and L5b, respectively. For this purpose, we injected the CTB555 into M2 sublayers by iontophoresis (Fig. 1*B*), and examined

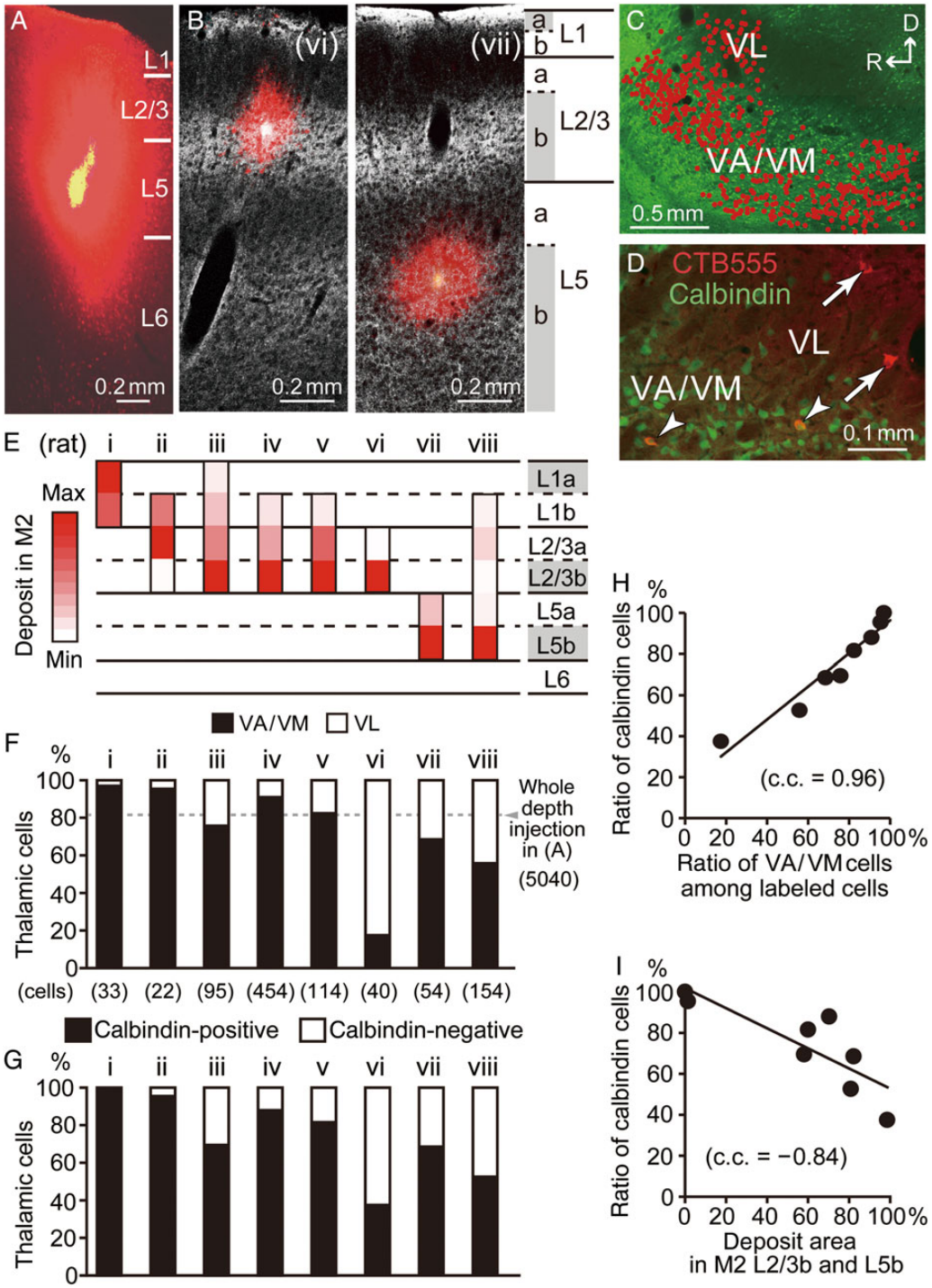

Figure 1. Laminar specificity of calbindin-positive and -negative thalamocortical inputs in the frontal cortex. (*A*) Massive Alexa Fluor 555-conjugated cholera toxin subunit B (CTB555) injection spanning L1 to upper L6 in secondary motor area (M2). (*B*) Localized CTB555 deposits in M2 (red; 2 cases shown). Gray scale image shows vesicular glutamate transporter type 2 (VGluT2) immunofluorescence, which presents denser VGluT2-positive puncta in layer (L) 1a, L2/3b, and L5b. Sagittal section, 20-μm thickness. Rat numbers (i–viii) are common in (*B* and *E*–*G*). (*C*) Retrogradely labeled thalamocortical cells by massive CTB555 injection shown in (*A*). Each red dot corresponds to a single labeled neuron. Ventral anterior/ventromedial (VA/VM) and ventrolateral (VL) nuclei were identified by additional calbindin immunostaining, showing stronger expression in VA/VM relative to VL. D, dorsal; R, rostral; Sagittal section (1.3 mm from the midline), 50-μm thickness. (*D*) Retrograde labeling of thalamocortical cells by iontophoretic injections of CTB555 into M2 (case viii in (*E*)). The VA/VM nuclei contain much more calbindin-positive cells than the VL nucleus. In accordance with calbindin cell distribution, labeled cells in VA/VM were mostly calbindin-positive (arrowheads), whereas those in VL were generally calbindin-negative (arrows). (*E*) Laminar localization of tracer deposits in M2. Color-coded scale, laminar proportions of the injection area from 0% (white) to the maximum (red) for individual injections. (*F*) Proportions of VA/VM and VL cells among the labeled thalamocortical cells. Black bar, VA/VM; white bar, VL. (n), total number of counted neurons. "Whole depth" indicates cells labeled by an extensive CTB555 injection, shown in (*A*). (*G*) Proportions of calbindin-positive and -negative cells among all labeled thalamocortical cells. Black bar, calbindin-positive; white bar, calbindin-negative. Note that the neuron populations are the same as those shown in (*F*). (*H*) Correlation between the ratio of calbindin-positive and VA/VM cells among the labeled cells ($P < 0.01$). c.c., correlation coefficient. (*I*) Negative correlations between the ratio of calbindin-positive cells among the labeled cells and the tracer deposit area proportions of L2/3b and L5b in the total deposit area ($P < 0.01$).

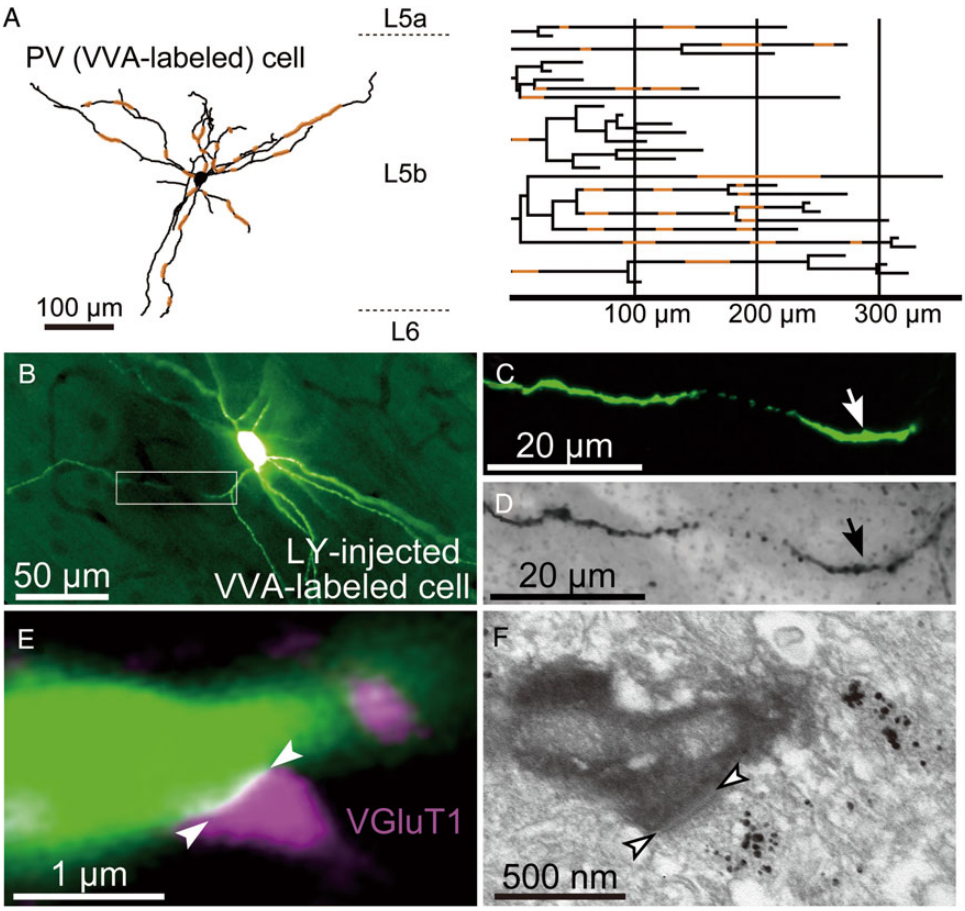

Figure 2. Appositions of VGluT-positive boutons on *Vicia villosa* agglutinin (VVA)-labeled dendrites. (*A*) Reconstruction (left) and dendrogram (right) of a VVA-labeled putative PV-positive cell in L5b that was intracellularly stained with Lucifer yellow (LY). The orange-colored segments are the dendritic regions used for measurements of VGluT-positive bouton appositions. (*B*) Fluorescent microscopic image of a VVA-labeled cell visualized by LY injection. (*C*) LY-labeled dendrite of the VVA cell, which corresponds to the segment enclosed by a square in (*B*). (*D*) The same dendritic part as (*C*) but visualized with a DAB immunoreaction against LY for subsequent EM observation. This section was also immunostained for VGluT1 by silver enhancement. (*E*) VGluT1-positive bouton apposition (magenta) on a VVA cell dendrite (green) visualized by immunofluorescence and LY injection. This dendritic segment corresponds to those indicated by arrows in (*C*) and (*D*). The region between the 2 arrowheads represents a bouton apposition site. (*F*) Synapse formation at the VGluT1-positive bouton apposition on the VVA cell dendrite, shown in (*E*). The electron-dense immunoreactions were used for LY (DAB) and VGluT1 (silver enhancement). The region between the 2 arrowheads indicates an asymmetric synapse on the dendrite, which corresponds to that in (*E*).

distributions of retrogradely labeled thalamic cells in the VA/VM nuclei and VL nucleus (Fig. 1*D*; 8 rats).

The proportion of calbindin-positive cells among the M2-projecting thalamic cells was 92.7% in the VA/VM nuclei ($n = 762$, 8 rats) and 19.1% in the VL nucleus ($n = 204$). The ratios of the calbindin-positive cells positively correlated with the ratios of labeled VA/VM cells [Fig. 1*H*; correlation coefficient (c.c.) = 0.96, $P < 0.01$].

By comparing labeling from layer-specific CTB555 injections with calbindin immunohistochemistry in individual labeled thalamic cells, we found a correlation of target laminae and calbindin expression in thalamocortical cells (Fig. 1*E–G*). When the injection site was restricted to L1 or L2/3a, almost all labeled thalamic cells were in the VA/VM nuclei [proportion of VA/VM cells, 97% in case i and 95.5% in case ii, which was larger than that when assuming nonselective innervation by VA/VM and VL thalamic cells (81.8%, dotted line in Fig. 1*F*; $P < 0.01$, χ^2 test)], and were positive for calbindin (proportion of calbindin-positive cells, 100% in case i and 95.5% in case ii; Fig. 1*G*).

On the other hand, when injections were biased to L2/3b or L5b, the number of labeled VL and calbindin-negative cells increased (proportion of VA/VM cells, 17.5% in case vi, 68.5% in case vii, and 55.8% in case viii, which was fewer than that when assuming nonselective innervation by VA/VM and VL thalamic cells [dotted line in Fig. 1*F*; $P < 0.05$ for case vii, $P < 0.01$ for cases vi and viii, χ^2 test]; proportion of calbindin-positive cells, 37.5% in case vi, 68.5% in case vii, and 52.6% in case viii; Fig. 1*G*). Finally, when injections were restricted to upper L6, few labeled cells were found in the thalamus, and all were positive for calbindin (data not shown).

Overall, the proportion of calbindin-positive cells among labeled thalamic cells was negatively correlated with the proportion of L2/3b and L5b within the tracer deposit area (Fig. 1*I*; c.c. = –0.84. $P < 0.01$). Importantly, L1-innervating thalamic cells were mostly positive for calbindin, while L2/3- and L5-innervating cells included both calbindin-positive and -negative cells. These results indicate that L2/3b and L5b receive thalamic inputs from both VA/VM and VL nuclei.

Glutamatergic Bouton Distributions along Dendrites of Pyramidal and PV Cells in L2/3b and L5b

Previous studies in rodents have demonstrated that the 2 major types of excitatory inputs can be discriminated by their selective

expression of different VGluTs: axonal boutons of cortical pyramidal cells express VGluT1, while those of thalamocortical fibers express VGluT2 (Fujiyama et al. 2001; Kubota et al. 2007 in this cortical area). To probe the synaptic input specificity among diverse presynaptic excitatory fibers arriving at different surface domains of cortical cell subtypes, we compared the distributions of presynaptic boutons that were positive for VGluT1 or VGluT2 between pyramidal and PV cells in L2/3b and L5b.

Dendritic arborizations of PV cells were visualized by LY injection into VVA-labeled cells, which correspond to PV-positive cells (Kosaka and Heizmann 1989; Ojima 1993; Kubota et al. 2011a). We reconstructed the dendrites of VVA cells (Fig. 2A; L2/3a, L2/3b, L5a, and L5b; 2 cells in each sublayer). The combination of LY intracellular staining with VGluT immunofluorescence allowed us to identify appositions between PV cell dendritic shafts and VGluT-positive boutons at various distances from the soma (Table 1).

We validated our apposition identification with EM observations of LY-injected dendrites combined with DAB immunostaining and VGluTs-labeled boutons with silver enhancement (Fig. 2B–E). Of the 19 apposing boutons identified using CLSM, 13 formed asymmetric synapses on target dendrites (Fig. 2E,F; probability: 68%). Four of the other six boutons formed asymmetric synapses on nonlabeled structures, and we could not find synaptic formations for the other 2 boutons.

Two L2/3b corticocortical pyramidal cells projecting to other cortical areas were intracellularly stained with LY injection. Since the apical dendritic tufts of L2/3b pyramidal cells were not stained due to technical limitation, only the basal and apical oblique dendrites were used for analysis. After reconstructing their dendrites (Fig. 3A, 2 cells), we used CLSM to identify VGluT1- and VGluT2-positive bouton appositions on the spines along dendritic segments at various distances from the soma (Table 1). The primary dendrites of L2/3b pyramidal cells were excluded from analysis.

L5 pyramidal cells of the rat frontal cortex comprise several projection subtypes (Morishima et al. 2011; Otsuka and Kawaguchi 2011; Ueta et al. 2014). One major subtype is CPn cells, which send axons to the ipsilateral pontine nuclei, while another is CCS cells, which bilaterally innervate the striatum (Fig. 3B). Since the apical dendrites of L5b pyramidal cells were only partially stained with LY injection, only the basal dendrites were used for analysis. The basal dendrites of retrogradely labeled CPn and CCS cells were visualized with intracellular LY injections (Fig. 3C). We reconstructed 2 L5b CPn and 2 CCS cells (Fig. 3B; Table 1) and identified VGluT1- and VGluT2-positive bouton appositions on spines along dendritic segments at various distances from the soma (Table 1). The primary dendrites of L5b pyramidal cells were excluded from the analysis.

We confirmed that VGluT1-positive bouton appositions made synapses on postsynaptic spines using conventional EM. We found that 24 of 27 (89%) appositions formed asymmetric synapses on target spines. To confirm dendritic representation of the fluorescence image of LY-filled cells, in addition to synaptic specialization, we used SBEM to consecutively reconstruct a dendritic segment of a CPn cell (Fig. 3C). This reconstruction conformed well to the stereoscopic image previously obtained using CLSM (Fig. 3D–I). We then were able to confirm 4 spine synapses among 6 spine contacts on the same dendritic segment using CLSM (Fig. 3J–P). These observations confirm that many CLSM-detected spine-apposing excitatory boutons form synapses on spines.

We compared glutamatergic apposition densities occurring at different distances from the soma and on target dendrites of

Table 1 Correlation of total VGluT densities with distances from somata

	Dendritic segments used for analysis				Total VGluT density versus distance			Total VGluT density versus diameter		
	N	Distance to segment center (range; µm)	Segment length (µm)	VGluT appositions (/segment)	Correlation coefficient	P	Regression coefficient $\times 10^{-2}$ (µm^{-2})	Correlation coefficient	P	Regression coefficient (µm^{-2})
Pyramidal dendritic spines										
L2/3b basal	22	36.4–190.3	25.9 ± 15.9	27.3 ± 16.7	0.11	n.s.	0.06	0.37	n.s.	0.29
L2/3b apical oblique	28	54.1–210.0	21.0 ± 13.1	19.0 ± 15.3	−0.35	n.s.	−0.18	0.67	<0.01	1.29
L5b CPn basal	40	38.9–343.0	12.9 ± 7.3	13.8 ± 8.4	0.01	n.s.	0.09	0.21	n.s.	0.18
L5b CCS basal	40	50.8–279.5	14.7 ± 11.0	16.0 ± 14.2	−0.32	<0.05	−0.15	0.21	n.s.	0.14
PV dendritic shafts										
L2/3a	49	4.1–191.7	13.8 ± 7.3	12.6 ± 6.8	−0.65	<0.05	−0.46	0.86	<0.01	1.66
L2/3b	35	5.4–279.5	13.6 ± 7.7	7.8 ± 5.1	−0.49	<0.01	−0.49	0.64	<0.01	0.87
L5a	23	15.5–395.0	26.0 ± 13.5	17.7 ± 16.7	−0.62	<0.01	−0.25	0.67	<0.01	1.11
L5b	42	6.6–358.1	22.6 ± 17.8	17.7 ± 16.6	−0.68	<0.01	−0.19	0.86	<0.01	0.90

Notes: *N* is the number of dendritic segments obtained from 2 cells.
P is the statistical significance of Pearson product-moment correlation coefficient; n.s., not significant.

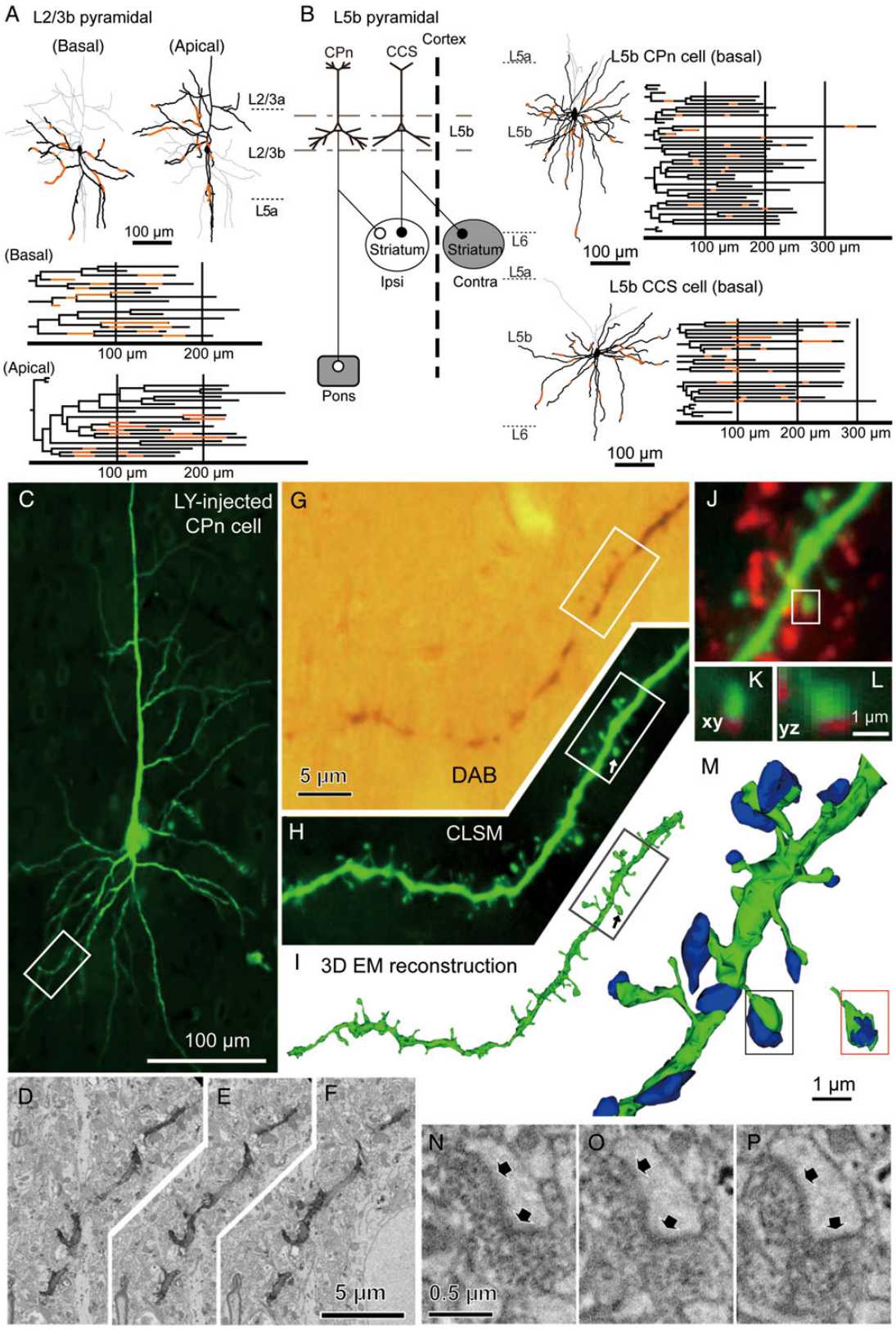

Figure 3. VGluT-positive axonal bouton appositions on spines of L2/3b and L5b pyramidal cells stained with LY. (*A*) Reconstructions of dendritic branches of a L2/3b corticocortical cell. Left, basal (black) and apical (gray); right, apical (black) and basal (gray). The neuron was visualized by intracellular injection of LY into a pyramidal cell labeled retrogradely from ipsilateral primary motor area. The dendrograms are shown below. Most basal dendritic branches were visualized by this labeling, but the apical branches were partially stained including oblique branches. The orange-colored segments were used for analysis. (*B*) Left: Identification of corticopontine (CPn) and crossed-corticostriatal (CCS) cells by retrograde labeling from the ipsilateral pontine nuclei and contralateral striatum (gray areas), respectively. Right: Reconstructions of the basal dendrites (black) and apical dendrites (gray) of LY-injected CPn (upper) and CCS cells (lower). The dendrograms of the basal dendrites are shown on the right.

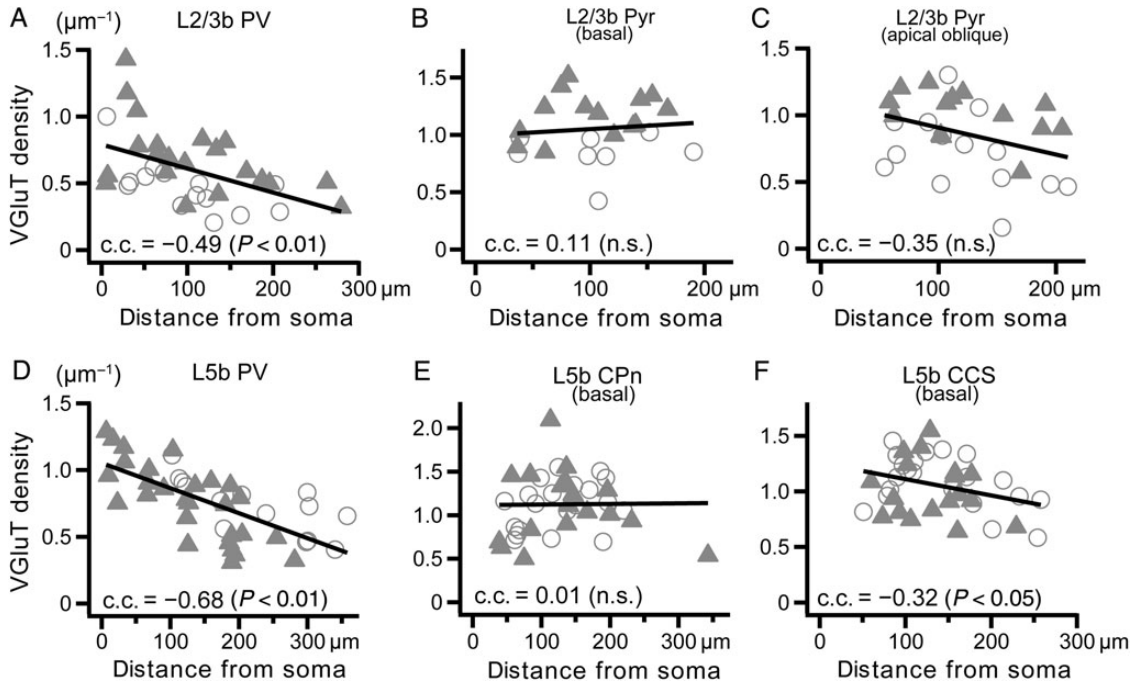

Figure 4. Relationship of the apposition densities of VGluT-labeled boutons with distances from the somata. (*A–C*) Relationship of VGluT-labeled bouton apposition densities on target dendrites in L2/3b with distances from the somata, obtained from 2 cells (open circles and filled triangles, respectively). (*A*) Dendritic shafts of PV cells; (*B*) basal dendritic spines of pyramidal cells; (*C*) apical oblique dendritic spines of pyramidal cells. Note that the densities of PV cells varied significantly depending on distance from the soma ($P < 0.01$), but those of pyramidal cells did not. n.s., statistically not significant. (*D–F*) Relationship of VGluT-labeled bouton apposition densities on target dendrite in L5b with distances from somata, obtained from 2 cells (open circles and filled triangles, respectively). (*D*) Dendritic shafts of PV cells; (*E*) basal dendritic spines of CPn cells; (*F*) basal dendritic spines of CCS cells. Note that the densities of PV and CCS cells varied depending on the distances significantly (PV cells, $P < 0.01$; CCS cells, $P < 0.05$), but those of CPn cells did not ($P = 0.93$).

different diameters, and compared these characteristics among the cell types. In L2/3b PV cells, the densities of VGluT-positive bouton appositions were negatively correlated with the distance from the soma (Fig. 4A), but were positively correlated with the target dendritic diameter (Supplementary Fig. 1A, Table 1). In L2/3b pyramidal cell dendrites, densities of VGluT-positive bouton appositions onto basal and apical oblique spines did not correlate with distance from the soma (Fig. 4B,C). The regression coefficient was more negative in apical oblique spines than basal spines (Table 1; $P < 0.05$, comparison of 2 regression parameters). Densities of VGluT-positive bouton appositions correlated with the dendritic shaft diameter in apical oblique spines, but not in basal spines (Supplementary Fig. 1B,C, Table 1).

In L5b, the densities of VGluT-positive bouton appositions to L5b PV cell dendrites were negatively correlated with distance from the soma (Fig. 4D), but positively with dendritic diameter (Supplementary Fig. 1D). VGluT-positive densities were differentially correlated with basal dendritic targets in 2 types of L5b pyramidal cell. The densities of VGluT-positive bouton appositions occurring on the basal spines of CPn cells did not correlate with either distance from the soma (Fig. 4E) or diameter (Supplementary Fig. 1E; Table 1), while densities of VGluT-positive bouton appositions were negatively correlated with distance from the soma (Fig. 4F), but independent of diameter, in CCS cell spines (Supplementary Fig. 1F, Table 1). Furthermore, correlations of VGluT-positive boutons with distance and diameter were much stronger in PV cell dendrites than in CCS cell spines (Table 1). Glutamatergic inputs to PV cells in other layers also showed strong correlations with both distance and diameter (Table 1).

These results suggest that distributions of glutamatergic terminals on the dendritic spines may be different between basal and apical oblique dendrites, and that those of L5b pyramidal cells are more dependent on cell surface location in

Orange-colored segments, the dendritic regions that were used for analysis. (*C*) A confocal laser scanning microscopy (CLSM) image of an LY-injected L5b pyramidal cell, identified as a CPn cell by retrograde labeling from the ipsilateral pontine nuclei. (*D–I*) Correspondence between morphologies of a dendritic segment imaged with CLSM and EM reconstructions. The segment shown corresponds to the dendrite in the rectangle in (*C*). (*D–F*) Diamond-knife serial block-face scanning electron microscope (SBEM) images obtained from the segment shown in (*G*). Z-step, 60 nm. (*G*) Bright field image of the segment shown in (*H*), visualized with DAB reaction. (*H*) Reconstruction from fluorescence images. (*I*) 3D reconstructions of the segment from SBEM images. (*J*) Dual fluorescence image of an LY-filled dendritic segment (green) and VGluT1 immunohistochemistry (red). This corresponds to the dendrite within the rectangle in (*H*). (*K* and *L*) The spine (green) is located just next to a VGluT1-positive axon terminal (red) in the *x–y* plane (*K*) as well as the *y–z* plane (*L*). This spine is the same one indicated by an arrow in (*H*) and within the rectangle in (*J*). (*M–P*) Confirmation of synapse formation at appositions identified by CLSM, correlating their EM images. From matching between dendritic morphologies of CLSM (*H*) and EM reconstructions (*I*), we could specify the spines and apposing boutons without presynaptic electron-dense staining. We confirmed synapse formation between the spine and apposing bouton (compare fluorescence images in (*J–L*), EM image reconstruction of the postsynaptic dendrite [green] and axon terminals [blue] in (*M*), and serial EM images of the synaptic junction on the spine (*N–P*), a region between 2 arrows, corresponding to the spine in the rectangle in (*M*). The junction area is shown within in the red rectangle, by rotating the spine and removing the presynaptic bouton.

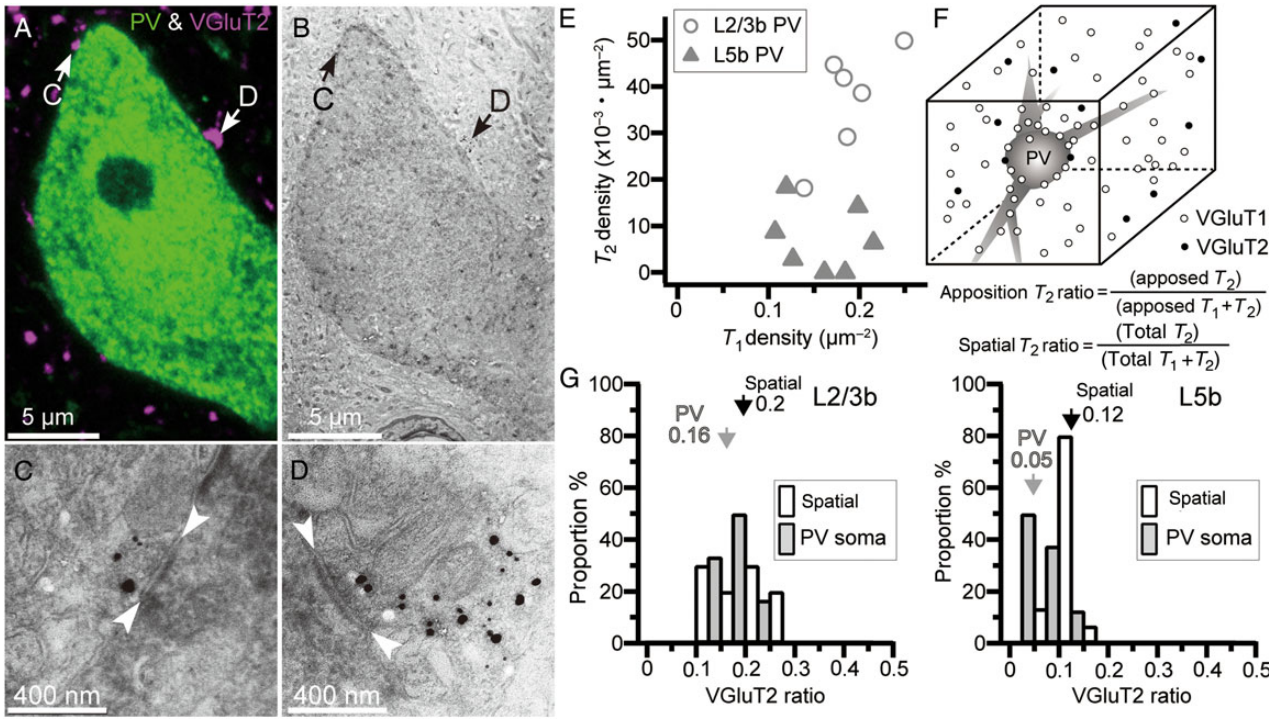

Figure 5. Bouton appositions of VGluT1/T2-positive terminals on PV-labeled somata. (*A–D*) Appositions and synapse formation of immunolabeled boutons on PV-labeled soma identified using CLSM and EM. (*A*) CLSM image of dual immunohistochemical staining of PV (green) and VGluT2 (magenta) in the frontal cortex. (*B*) Lower magnification EM image of the identical neuron in (*A*) visualized by DAB staining and VGluT2-positive boutons visualized by silver enhancement. (*C* and *D*) Higher magnification EM images of VGluT2-positive boutons obtained from a section adjacent to that of (*B*). Both boutons apposing on a PV-labeled soma identified by CLSM made synapses on the target soma (region between the 2 white arrowheads, synaptic junction). (*E*) Density comparison of VGluT1/T2-labeled boutons apposing on PV-labeled somata between L2/3b and L5b. Open circle, L2/3b; filled triangle, L5b. (*F*) Spatial T_2 ratio: ratio of VGluT2-positive boutons to whole VGluT-positive boutons in the local environment. Apposition T_2 ratio: ratio of VGluT2 appositions to total glutamatergic appositions. (*G*) VGluT2-labeled boutons among all VGluT-labeled boutons (VGluT2 ratio) in L2/3b (left) and L5b (right). White bar, spatial T_2 ratio; Gray bar, apposition T_2 ratio. Arrows, mean value. The apposition T_2 ratios of L2/3b PV somata were similar to the spatial T_2 ratio in L2/3b, but those of L5b PV somata were lower than the spatial T_2 ratio in L5b ($P < 0.01$, Mann–Whitney *U*-test).

Table 2 VGluT appositions onto PV somata

	VGluT1 density (μm^{-2})	Estimated total number	VGluT2 density (μm^{-2})	Estimated total number
L2/3a	0.21 ± 0.05 (n = 11)	113.3 ± 38.2	0.01 ± 0.01 (n = 11)	3.8 ± 3.8
L2/3b	0.22 ± 0.08 (n = 11)	121.0 ± 38.0	0.04 ± 0.03** (n = 14)	21.8 ± 10.2**
L5a	0.22 ± 0.05 (n = 11)	120.5 ± 41.9	0.02 ± 0.02 (n = 10)	10.1 ± 8.6
L5b	0.19 ± 0.06 (n = 11)	135.3 ± 41.9	0.01 ± 0.01 (n = 10)	8.2 ± 6.3
L6	0.21 ± 0.04 (n = 10)	129.5 ± 28.8	0.01 ± 0.01 (n = 11)	5.5 ± 2.3

Notes: Estimated total number, estimated total number of each VGluT-positive bouton apposing on individual somata assuming the prolate spheroid shapes.
**$P < 0.01$, post hoc Tukey–Kramer test.

postsynaptic CCS cell dendrites relative to CPn cell dendrites. In addition, glutamatergic terminal distributions on dendrites are more dependent on the target properties (distance and diameter) of PV cells than pyramidal cells in both L2/3b and L5b.

Glutamatergic Bouton Apposition Density and Thalamic Input Ratio over PV Somata

PV cells receive excitatory inputs not only along dendrites but also over somata. Therefore, we compared glutamatergic inputs over PV somata between cortical sublayers. First, we confirmed that 17 boutons out of the 20 apposing boutons formed asymmetrical synapses on the target PV somata (85%; Fig. 5*A–D*). The other 3 boutons formed asymmetrical synapses on nonlabeled neural structures. So we assumed that most of the apposing boutons on PV somata observed by CLSM form synapses with the soma.

We derived apposing bouton densities from the number of apposing boutons and surface area of partially reconstructed PV somata. The surface densities of VGluT1-positive bouton appositions (T_1 apposition densities) on PV somata were similar across sublayers (Table 2). VGluT2 apposition densities (T_2 apposition densities) on PV somata were much lower than T_1 densities in all sublayers (Table 2). We estimated the total number of VGluT-positive bouton appositions in individual somata, assuming an ellipsoidal cell body. The total number of somatic appositions for VGluT1-positive boutons was similar among the sublayers (Table 2). The total number for VGluT2-positive boutons was larger in L2/3b (22 ± 10 boutons) than in the other sublayers ($P < 0.01$; Table 2).

We further compared glutamatergic inputs on PV somata between L2/3b and L5b. T_1 apposition densities on PV somata were not different between L2/3b and L5b ($P = 0.57$; Table 2). On the

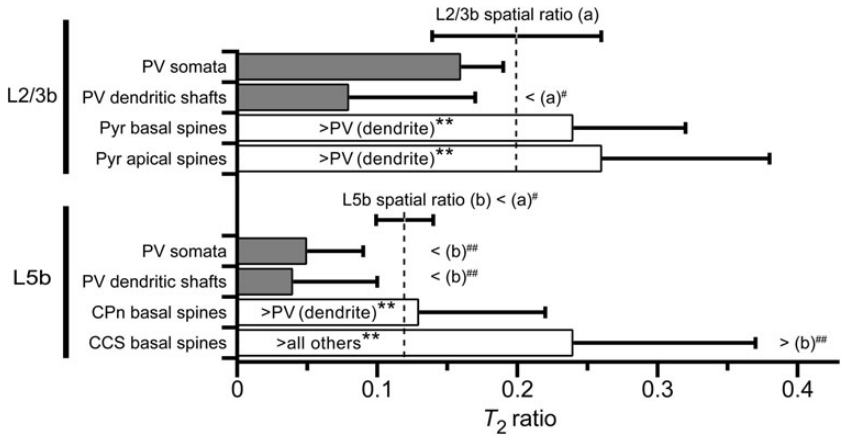

Figure 6. Apposition T_2 ratios in L2/3b and L5b cell subtypes and comparison with the spatial T_2 ratio. Gray bars, apposition T_2 ratios in somata and dendritic shafts of PV cells; white bars, apposition T_2 ratios in dendritic spines of pyramidal cells. Horizontal bar, mean + SD. Comparison among the subtypes and domains by Tukey–Kramer test: $^{*}P < 0.05$ and $^{**}P < 0.01$. Vertical dashed lines, mean of spatial T_2 ratios: VGluT2-labeled boutons among total VGluT-labeled boutons (both VGluT1 and VGluT2) distributed locally; (a) for L2/3b and (b) for L5b. Comparison between the apposition and spatial T_2 ratios by Mann–Whitney *U*-tests: $^{\#}P < 0.05$ and $^{\#\#}P < 0.01$.

other hand, T_2 apposition densities were larger in L2/3b than in L5b ($P < 0.01$; Fig. 5*E*, Table 2). The ratios of VGluT2 appositions to total glutamatergic appositions (apposition T_2 ratios, Fig. 5*F*) were higher in L2/3b PV somata (0.16 ± 0.03, $n = 6$) than in L5b PV somata (0.05 ± 0.04, $n = 8$; $P < 0.01$).

Apposition T_2 ratios would likely be affected by individual cell preferences for thalamic inputs, as well as relative local proportion of thalamocortical fibers among all glutamatergic afferents. To estimate the latter effect, we obtained the ratios of VGluT2-positive boutons to all VGluT-positive boutons in the local environment (spatial T_2 ratios, Fig. 5*F*). Spatial T_2 ratios were higher in L2/3b (0.20 ± 0.06; 10 rectangular cubes, 512.5 ± 206.6 μm^3) than in L5b ($P < 0.05$; 0.12 ± 0.02; 15 rectangular cubes, 548.8 ± 248.4 μm^3; Fig. 5*G*, 6). If an apposition T_2 ratio was higher than the spatial T_2 ratio in a given space, that neuronal domain would preferentially receive VGluT2-positive inputs relative to VGluT1-positive inputs; if it was lower, that domain would avoid otherwise available VGluT2-positive inputs. Therefore, we compared apposition T_2 ratios for individual domains with the spatial T_2 ratio. Apposition T_2 ratios of L2/3b PV somata were similar to L2/3b spatial T_2 ratios ($P = 0.21$; Fig. 5*G* left, Fig. 6). On the other hand, apposition T_2 ratios of L5b PV somata were lower than L5b spatial T_2 ratio ($P < 0.01$; Fig. 5*G* right, Fig. 6). These results suggest that L2/3b PV somata receive thalamocortical inputs in proportion to the relative abundance of local thalamic boutons, whereas PV somata in L5b prefer corticocortical inputs over thalamic afferents.

Thalamic Input Ratio Comparison among the Cell Subtypes and Surface Domains in L2/3b and L5b

In addition to PV somata, we extended thalamic input preference analysis to dendritic domains of PV and pyramidal cells in L2/3b, and PV, CPn, and CCS cells in L5b, using apposition and spatial T_2 ratios. In L2/3b, apposition T_2 ratios of PV somata (0.16 ± 0.03), basal spines (0.24 ± 0.08), and apical oblique spines (0.26 ± 0.12) of pyramidal cell dendrites were not different, and were similar to the local spatial T_2 ratio (Fig. 6). On the other hand, apposition T_2 ratios of PV dendritic shafts (0.08 ± 0.09) were lower than those of pyramidal spines ($P < 0.01$), and were lower than the L2/3b spatial T_2 ratio ($P < 0.05$; Fig. 6).

In L5b, apposition T_2 ratios of PV somata (0.05 ± 0.04) and dendrites (0.04 ± 0.06) were lower than the local spatial T_2 ratio (Fig. 6). Apposition T_2 ratios of basal dendritic spines in CPn cells (0.13 ± 0.09) were similar to the spatial T_2 ratio, whereas those in CCS cells (0.24 ± 0.13) were higher than the L5b spatial T_2 ratio as well as those in CPn cells (Fig. 6). Thus, among the pyramidal cells examined, dendritic spines of CCS cells received a higher proportion of thalamic inputs. Among PV surface domains, L2/3b somata received preferential innervation by thalamic inputs.

As above, thalamic input ratios with respect to total glutamatergic input varied between cell subtypes and surface domains. Glutamatergic input densities along dendrites were dependent on distance from the soma in specific cell subtypes (Fig. 4). Therefore, we further compared the input densities between proximal (within 100 μm) and distal (further than 125 μm from the soma) dendritic regions.

In L2/3b, T_1 apposition densities on PV dendrites were higher in proximal (0.62 ± 0.22/μm) than in distal (0.45 ± 0.13/μm) dendrites, whereas at pyramidal cell dendrites, densities were similar in proximal (basal, 0.84 ± 0.23/μm; apical oblique, 0.65 ± 0.17/μm) and in distal (basal, 0.85 ± 0.17/μm; apical oblique, 0.55 ± 0.26/μm) regions (Fig. 7*A* upper, Supplementary Table 1). The T_1 apposition densities in distal regions were higher in pyramidal basal spines than both in PV dendritic shafts and in pyramidal apical oblique spines (Fig. 7*A* upper).

In L2/3b, dendritic shafts of PV cells showed similar T_2 apposition densities between proximal (0.09 ± 0.10/μm) and distal (0.03 ± 0.06/μm) dendritic regions (Fig. 7*A* lower, Supplementary Table 1). Pyramidal basal spines also showed similar T_2 apposition densities between proximal (0.20 ± 0.09/μm) and distal (0.29 ± 0.06/μm) regions, but T_2 apposition densities of apical oblique spines were larger in proximal (0.28 ± 0.14/μm) than in distal (0.12 ± 0.10/μm) regions. The T_2 apposition densities in proximal regions were higher in pyramidal apical oblique spines than in PV dendritic shaft (Fig. 7*A* lower). The T_2 apposition densities in distal dendritic regions were overall higher in pyramidal spines than in PV dendrites, and higher in basal spines than in apical oblique spines (Fig. 7*A* lower).

In L5b, T_1 apposition densities in PV dendrites were more pronounced in proximal (0.93 ± 0.16/μm) dendrites than in distal (0.59 ± 0.19/μm) regions (Fig. 7*B* upper, Supplementary Table 1). Dendritic spines of CPn cells showed similar T_1 apposition densities between in proximal (0.86 ± 0.36/μm) and distal (0.98 ± 0.24/μm) regions, while CCS cell spines had larger T_1

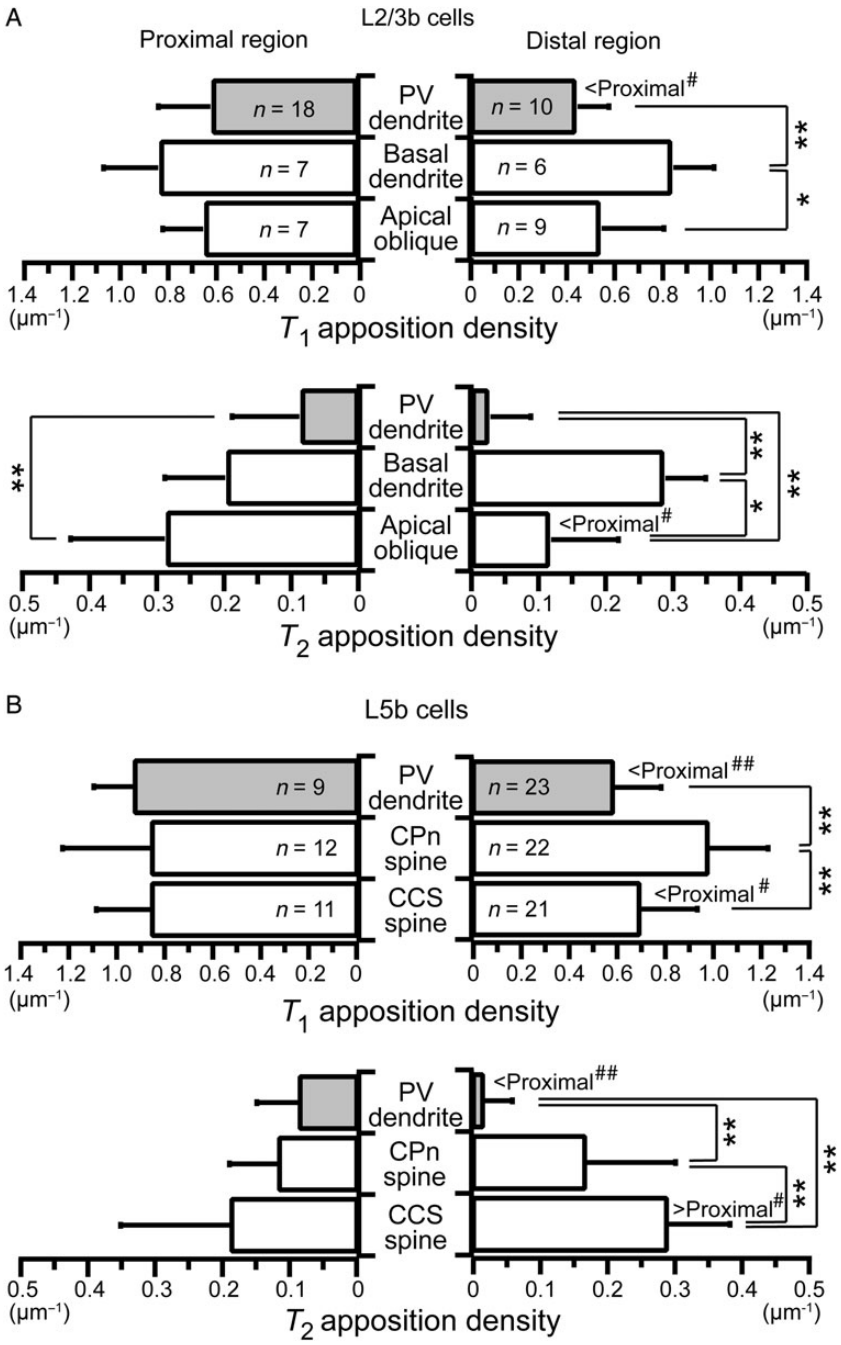

Figure 7. Bouton apposition densities of VGluT1/T2-positive terminals on dendritic regions proximal and distal from the soma. (A) T_1/T_2 apposition densities of L2/3b cells. Gray bars, apposition densities of PV cell dendritic shafts; white bars, apposition densities of pyramidal cell spines. Data, mean + SD. Segments with the dendritic regions nearer than 100 μm (left, proximal region) and further than 125 μm (right, distal region) were used. Upper, T_1 apposition density; lower, T_2 apposition density. Proximal/distal comparisons by Mann–Whitney U-tests ($^{\#}P < 0.05$ and $^{\#\#}P < 0.01$); subtype comparisons by Tukey–Kramer tests ($^{*}P < 0.05$ and $^{**}P < 0.01$). (B) T_1/T_2 apposition densities of L5b cells. Gray bars, apposition densities of PV cell dendritic shafts; white bars, apposition densities of CPn and CCS cell spines. Segments with the dendritic regions nearer than 100 μm (left, proximal region) and further than 125 μm (right, distal region) were used.

apposition densities in proximal (0.86 ± 0.22/μm) dendrites than in distal (0.70 ± 0.23/μm) regions (Fig. 7*B* upper). There was no difference in proximal T_1 apposition densities among these 3 cell subtypes, but T_1 apposition densities were higher in distal dendritic spines of CPn cells (Fig. 7*B* upper).

In L5b, T_2 apposition densities in PV dendrites were larger in proximal (0.09 ± 0.06/μm) relative to distal (0.02 ± 0.04/μm) dendrites (Fig. 7*B* lower, Supplementary Table 1). Dendritic spines of CPn cells showed similar T_2 apposition densities at proximal (0.12 ± 0.07/μm) and distal (0.17 ± 0.13/μm) locations, while dendritic spines of CCS cells showed larger densities in distal (0.29 ± 0.09/μm) regions relative to more proximal (0.19 ± 0.16/μm) domains (Fig. 7*B* lower). There was no difference in T_2 apposition densities in proximal dendrites of these 3 cell subtypes, but T_2 apposition densities were highest in distal spines of CCS cells, and lowest in distal dendritic shafts of PV cells (Fig. 7*B* lower). Thus,

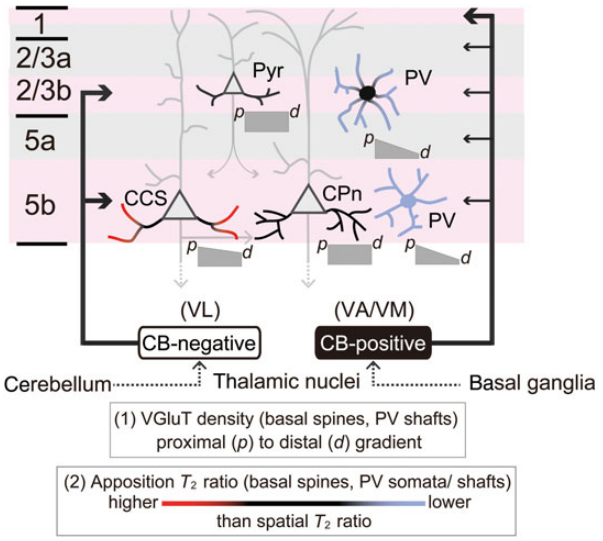

Figure 8. Local excitatory input selectivity depends on presynaptic cell type, as well as on postsynaptic cell subtype and surface domain. Calbindin-positive thalamocortical fibers innervate L1 and, to a lesser extent, all other layers. On the other hand, calbindin-negative thalamocortical fibers preferentially innervate L2/3b and L5b. In L2/3b, the dendrites of pyramidal cells and somata of PV cells receive thalamic inputs in proportion to their local abundance among all excitatory terminals (represented by black color), while dendrites of PV cells avoid otherwise available thalamic inputs (represented by blue color). In L5b, CCS cell basal dendrites, particularly their distal parts, receive more thalamic inputs than predicted by their local abundance (represented by red color), whereas both somata and dendrites of PV cells repel thalamic inputs. The density of VGluT-positive all excitatory inputs onto PV cell dendritic shafts and CCS cell spines decreases with distance from soma, while excitatory input density on CPn cell spines is independent of distance from soma.

among L5b dendrites, relative to pyramidal cells, fewer thalamic inputs target PV cells, preferring instead dendritic spines of CCS cells, especially those in distal dendrites.

Discussion

In the present study, the distribution patterns of corticocortical and thalamocortical excitatory synaptic inputs were investigated among identified postsynaptic cortical cell subtypes using intracellular and immunohistochemical staining combined with CLSM and EM observations of post- and presynaptic elements. Our results indicate that cortical neurons are innervated by thalamic fibers in a selective manner that is dependent on their laminar position, cell subtype, and surface domain in the rat frontal cortex (Fig. 8).

Thalamic Inputs to L2/3b Cells

Thalamic inputs were more frequently found in the proximal portions of apical oblique dendrites of L2/3b pyramidal cells. These finding are consistent with a proposal that synaptic strength decreases along the length of each apical oblique branch of hippocampal CA1 pyramidal cells (Katz et al. 2009). We previously reported that spines innervated by thalamocortical fibers are larger, and have wider synaptic junctional areas, than spines receptive to corticocortical inputs in the rat frontal cortex, suggesting that thalamocortical inputs are stronger and more reliable than corticocortical inputs (Kubota et al. 2007). Together, thalamic inputs to proximal thicker dendrites may require precise temporal coincidence for summation, whereas distal dendrites can integrate corticocortical inputs in wider time window, dependent on dendritic nonlinearities and impedance gradients (Branco and Häusser 2011).

In spiny stellate cells in L4 of somatosensory areas, a heavily thalamorecipient layer, thalamic inputs arrive at locations more proximal to the soma than do corticocortical inputs (Jia et al. 2014; Schoonover et al. 2014). Thus, thalamocortical targeting of soma-proximal dendritic domains may be a conserved feature in some dendritic branches of neurons in the thalamorecipient midlayer across cortical areas. However, the basal dendrites of L2/3b pyramidal cells received both cortical and thalamic inputs in proportion to their relative local abundance, irrespective of distance from the soma. These data suggest that thalamic input integration or interaction with cortical inputs is different between basal and apical oblique dendrites.

Glutamatergic terminal distributions were different between pyramidal and PV cells. Excitatory input densities on L2/3b pyramidal spines were relatively independent of distance from the somata. On the other hand, the density of glutamatergic inputs to PV cell dendrites decreased according to their distance from the soma, a main determinant of efficacy of synaptic signal transmission to the soma (Kubota et al. 2011b). The somata of L2/3b PV cells received thalamic inputs in proportion to their relative abundance in the local environment, whereas PV-positive dendrites showed a preference for cortical inputs over otherwise available thalamic afferents (Kameda et al. 2012). This indicates that the thalamic inputs to L2/3b PV cells are weighted to soma-proximal dendritic domains.

PV-positive fast-spiking (FS) basket cells are phasically activated by fast excitatory inputs on the soma (Nörenberg et al. 2010). In L4 of primary sensory areas, FS cells receive stronger thalamocortical inputs than neighboring excitatory cells, and fire early in the initial stages of neocortical processing (Agmon and Connors 1992; Beierlein et al. 2003; Cruikshank et al. 2007; Hull and Scanziani 2007; Kimura et al. 2010; Kloc and Maffei 2014). Therefore, cerebellar outputs relayed by the thalamic VL nucleus may excite L2/3b cells in a temporally restricted manner achieved via fast feedforward inhibition exerted by PV cells.

M2 L2/3b PV cells are thought to participate in induction of cortical gamma oscillations (Hu et al. 2014) and synchronization of firing among pyramidal cells projecting to the adjacent primary motor area as well as to L5 pyramidal cells in M2 (Ueta et al. 2014). The reciprocal connections between PV and pyramidal cells are crucial for generation of the gamma oscillation (Bartos et al. 2007). Since loss of PV expression, especially in the superficial layers of the frontal cortex, and reduction of gamma oscillations are pathophysiological hallmarks of schizophrenia, impaired PV function may contribute to this disease (Hashimoto et al. 2003; Marín 2012; Uhlhaas and Singer 2012; Lewis 2014; Cho et al. 2015). Thus, L2/3b PV cells may participate in both the fast feedforward inhibition caused by thalamocortical inputs and the generation of gamma oscillations in cooperation with nearby pyramidal cells.

L5b Cells Receiving Excitation from Thalamic and L2/3b Cells

Unlike PV cells in L2/3b, L5b PV cells preferentially received corticocortical inputs at both somatic and dendritic locations. This result suggests that the composition of excitatory input to PV cells is determined primarily by laminar location.

On the other hand, the patterns of excitatory inputs onto pyramidal cells in L5b were dependent on cell subtype. In L5b CPn cells, similar to L2/3b pyramidal cells, the density of

glutamatergic input on basal dendritic spines was independent of distance from the soma. Conversely, in L5b CCS cells, the density of excitatory input to the basal dendrites decreased with distance from the soma. This may be related to the differences in synaptic integration at the distal basal dendrites between the 2 pyramidal cell subtypes.

Dendritic spines of CPn cells received thalamic inputs in proportion to their local abundance in both proximal and distal regions; however, CCS cell spines were preferentially receptive to thalamic terminals, particularly in their distal dendritic locations, opposite of the apical oblique branches of L2/3b pyramidal cells. Considering the avoidance of thalamic inputs onto L5b PV cells, thalamocortical terminals appear to be highly selective in targeting surface subdomains on specific cortical neuron subclasses, even within the same cortical sublamina.

L5b CPn cells are most responsive to spatially distributed inputs within a narrow time window (Dembrow et al. 2015). L2/3b pyramidal cells are thought to fire fast and transiently in response to thalamocortical inputs, due to rapid feedforward inhibition from PV cells. Since L2/3b pyramidal cells innervate L5b CPn cells (Otsuka and Kawaguchi 2008), it is possible that L5b CPn cells receive bursts of temporally coordinated inputs from L2/3b pyramidal cells over a short duration following direct thalamocortical input to superficial cortical layers.

L5b CCS cells are also innervated by L2/3b pyramidal cells (Otsuka and Kawaguchi 2008), and received thalamic inputs more in distal dendrites than in proximal dendrites. Distal dendritic inputs exhibit an input–output function having a higher gain and a broader window, due to slower time constants and response nonlinearities such as NMDA spikes, than proximal dendritic inputs do to the same dendrite (Nevian et al. 2007; Branco and Häusser 2011; Major et al. 2013). Thus, CCS cells may integrate direct thalamic inputs and indirect inputs via L2/3b cells with dispersed firing times (Dembrow et al. 2015).

Calbindin-negative thalamic VL cells receive cerebellar outputs from the dentate nucleus (Deniau et al. 1992; Jones 2007; Kuramoto et al. 2011), and innervate mostly L2/3b and L5b. L5b CPn cells would be fired by conjoint direct and indirect inputs via L2/3b pyramidal cells caused by synchronous activation of cerebellar-driven thalamic cells. In contrast, if thalamic VL cells increased firing gradually, their excitatory postsynaptic potentials would integrate slowly in CCS cells over a relatively wide temporal window, followed by delayed excitation of CPn cells via unidirectional excitatory input from CCS cells (Morishima and Kawaguchi 2006). Following excitatory drive from the cerebellum-driven thalamic nucleus, CPn cells may have 2 temporal modes of outputs to the thalamus, pontine nuclei, and spinal cord: a fast, temporally precise mode, and a slower mode with greater input integration.

Conclusion

We show an exquisite selectivity among thalamocortical afferents in which synaptic connectivity is dependent on the postsynaptic cell subtype, cortical sublayer, and cell surface domain. The dendrites of PV cells preferentially receive corticocortical inputs in both sublayers. The somata of L2/3b PV cells receive thalamic inputs with similar proportions to the dendritic spines of L2/3b pyramidal cells, whereas the somata of L5b PV cells are mostly innervated by cortical inputs. The basal dendrites of L2/3b pyramidal cells receive both cortical and thalamic inputs in proportion to their relative local abundance, whereas thalamic input densities of apical oblique dendrites were fewer at more distant branches. L5b CPn cells receive glutamatergic inputs in proportion to their local abundance, whereas L5b CCS cells show a preference for thalamic inputs, particularly in their distal dendrites. Based on the connectional specificity of thalamic innervation among the cortical cell subtypes, the frontal cortex may process inputs from cerebellar-driven thalamic cells differently according to their firing patterns.

Supplementary Material

Supplementary material can be found at: http://www.cercor.oxfordjournals.org.

Funding

This work was supported by JST, CREST, and Grant-in-Aids for Scientific Research from the Ministry of Education, Culture, Sports, Science, and Technology (MEXT; No. 25250005, 26120730, 15K14324, and 15H01456).

Notes

We thank Noboru Yamaguchi and Ryoko Narimatsu for histological assistance, and Allan T. Gulledge, Yasuharu Hirai, and Fuyuki Karube for comments on the manuscript. *Conflict of Interest*: None declared.

References

Agmon A, Connors BW. 1992. Correlation between intrinsic firing patterns and thalamocortical synaptic responses of neurons in mouse barrel cortex. J Neurosci. 12:319–329.

Avesar D, Gulledge AT. 2012. Selective serotonergic excitation of callosal projection neurons. Front Neural Circuits. 6:12.

Bartos M, Vida I, Jonas P. 2007. Synaptic mechanisms of synchronized gamma oscillations in inhibitory interneuron networks. Nat Rev Neurosci. 8:45–56.

Beierlein M, Gibson JR, Connors BW. 2003. Two dynamically distinct inhibitory networks in layer 4 of the neocortex. J Neurophysiol. 90:2987–3000.

Benshalom G, White EL. 1986. Quantification of thalamocortical synapses with spiny stellate neurons in layer IV of mouse somatosensory cortex. J Comp Neurol. 253:303–314.

Branco T, Häusser M. 2011. Synaptic integration gradients in single cortical pyramidal cell dendrites. Neuron. 69:885–892.

Cho KK, Hoch R, Lee AT, Patel T, Rubenstein JL, Sohal VS. 2015. Gamma rhythms link prefrontal interneuron dysfunction with cognitive inflexibility in Dlx5/6+/– mice. Neuron. 85:1332–1343.

Constantinople CM, Bruno RM. 2013. Deep cortical layers are activated directly by thalamus. Science. 340:1591–1594.

Cruikshank SJ, Lewis TJ, Connors BW. 2007. Synaptic basis for intense thalamocortical activation of feedforward inhibitory cells in neocortex. Nat Neurosci. 10:462–468.

da Costa NM, Martin KA. 2011. How thalamus connects to spiny stellate cells in the cat's visual cortex. J Neurosci. 31:2925–2937.

DeFelipe J, Fariñas I. 1992. The pyramidal neuron of the cerebral cortex: morphological and chemical characteristics of the synaptic inputs. Prog Neurobiol. 39:563–607.

Dembrow NC, Zemelman BV, Johnston D. 2015. Temporal dynamics of L5 dendrites in medial prefrontal cortex regulate integration versus coincidence detection of afferent inputs. J Neurosci. 35:4501–4514.

Deniau JM, Kita H, Kitai ST. 1992. Patterns of termination of cerebellar and basal ganglia efferents in the rat thalamus. Strictly segregated and partly overlapping projections. Neurosci Lett. 144:202–206.

Fiala JC. 2005. Reconstruct: a free editor for serial section microscopy. J Microsc. 218:52–61.

Fujiyama F, Furuta T, Kaneko T. 2001. Immunocytochemical localization of candidates for vesicular glutamate transporters in the rat cerebral cortex. J Comp Neurol. 435:379–387.

Gibson JR, Beierlein M, Connors BW. 1999. Two networks of electrically coupled inhibitory neurons in neocortex. Nature. 402:75–79.

Graziano A, Liu XB, Murray KD, Jones EG. 2008. Vesicular glutamate transporters define two sets of glutamatergic afferents to the somatosensory thalamus and two thalamocortical projections in the mouse. J Comp Neurol. 507:1258–1276.

Gulyás AI, Acsády L, Freund TF. 1999. Structural basis of the cholinergic and serotonergic modulation of GABAergic neurons in the hippocampus. Neurochem Int. 34:359–372.

Hashimoto T, Volk DW, Eggan SM, Mirnics K, Pierri JN, Sun Z, Sampson AR, Lewis DA. 2003. Gene expression deficits in a subclass of GABA neurons in the prefrontal cortex of subjects with schizophrenia. J Neurosci. 23:6315–6326.

Hirai Y, Morishima M, Karube F, Kawaguchi Y. 2012. Specialized cortical subnetworks differentially connect frontal cortex to parahippocampal areas. J Neurosci. 32:1898–1913.

Hu H, Gan J, Jonas P. 2014. Interneurons. Fast-spiking, parvalbumin^{+} GABAergic interneurons: from cellular design to microcircuit function. Science. 345:1255263.

Hull C, Scanziani M. 2007. It's about time for thalamocortical circuits. Nat Neurosci. 10:400–402.

Jia H, Varga Z, Sakmann B, Konnerth A. 2014. Linear integration of spine Ca^{2+} signals in layer 4 cortical neurons in vivo. Proc Natl Acad Sci USA. 111:9277–9282.

Jones EG. 2009. Synchrony in the interconnected circuitry of the thalamus and cerebral cortex. Ann N Y Acad Sci. 1157: 10–23.

Jones EG. 2007. The thalamus. 2nd ed. Cambridge (UK): Cambridge University Press.

Kameda H, Hioki H, Tanaka YH, Tanaka T, Sohn J, Sonomura T, Furuta T, Fujiyama F, Kaneko T. 2012. Parvalbumin-producing cortical interneurons receive inhibitory inputs on proximal portions and cortical excitatory inputs on distal dendrites. Eur J Neurosci. 35:838–854.

Katz Y, Menon V, Nicholson DA, Geinisman Y, Kath WL, Spruston N. 2009. Synapse distribution suggests a two-stage model of dendritic integration in CA1 pyramidal neurons. Neuron. 63:171–177.

Kawaguchi Y, Wilson CJ, Emson PC. 1989. Intracellular recording of identified neostriatal patch and matrix spiny cells in a slice preparation preserving cortical inputs. J Neurophysiol. 62:1052–1068.

Kimura F, Itami C, Ikezoe K, Tamura H, Fujita I, Yanagawa Y, Obata K, Ohshima M. 2010. Fast activation of feedforward inhibitory neurons from thalamic input and its relevance to the regulation of spike sequences in the barrel cortex. J Physiol. 588:2769–2787.

Kloc M, Maffei A. 2014. Target-specific properties of thalamocortical synapses onto layer 4 of mouse primary visual cortex. J Neurosci. 34:15455–15465.

Kosaka T, Heizmann CW. 1989. Selective staining of a population of parvalbumin-containing GABAergic neurons in the rat cerebral cortex by lectins with specific affinity for terminal N-acetylgalactosamine. Brain Res. 483:158–163.

Kubota Y, Hatada S, Kondo S, Karube F, Kawaguchi Y. 2007. Neocortical inhibitory terminals innervate dendritic spines targeted by thalamocortical afferents. J Neurosci. 27: 1139–1150.

Kubota Y, Karube F, Nomura M, Gulledge AT, Mochizuki A, Schertel A, Kawaguchi Y. 2011b. Conserved properties of dendritic trees in four cortical interneuron subtypes. Sci Rep. 1:89.

Kubota Y, Shigematsu N, Karube F, Sekigawa A, Kato S, Yamaguchi N, Hirai Y, Morishima M, Kawaguchi Y. 2011a. Selective coexpression of multiple chemical markers defines discrete populations of neocortical GABAergic neurons. Cereb Cortex. 21:1803–1817.

Kuramoto E, Fujiyama F, Nakamura KC, Tanaka Y, Hioki H, Kaneko T. 2011. Complementary distribution of glutamatergic cerebellar and GABAergic basal ganglia afferents to the rat motor thalamic nuclei. Eur J Neurosci. 33:95–109.

Kuramoto E, Furuta T, Nakamura KC, Unzai T, Hioki H, Kaneko T. 2009. Two types of thalamocortical projections from the motor thalamic nuclei of the rat: a single neuron-tracing study using viral vectors. Cereb Cortex. 19:2065–2077.

Lewis DA. 2014. Inhibitory neurons in human cortical circuits: substrate for cognitive dysfunction in schizophrenia. Curr Opin Neurobiol. 26:22–26.

Major G, Larkum ME, Schiller J. 2013. Active properties of neocortical pyramidal neuron dendrites. Annu Rev Neurosci. 36:1–24.

Marín O. 2012. Interneuron dysfunction in psychiatric disorders. Nat Rev Neurosci. 13:107–120.

Matsubara JA, Chase R, Thejomayen M. 1996. Comparative morphology of three types of projection-identified pyramidal neurons in the superficial layers of cat visual cortex. J Comp Neurol. 366:93–108.

Morishima M, Kawaguchi Y. 2006. Recurrent connection patterns of corticostriatal pyramidal cells in frontal cortex. J Neurosci. 26:4394–4405.

Morishima M, Morita K, Kubota Y, Kawaguchi Y. 2011. Highly differentiated projection-specific cortical subnetworks. J Neurosci. 31:10380–10391.

Nevian T, Larkum ME, Polsky A, Schiller J. 2007. Properties of basal dendrites of layer 5 pyramidal neurons: a direct patch-clamp recording study. Nat Neurosci. 10:206–214.

Nörenberg A, Hu H, Vida I, Bartos M, Jonas P. 2010. Distinct nonuniform cable properties optimize rapid and efficient activation of fast-spiking GABAergic interneurons. Proc Natl Acad Sci USA. 107:894–899.

Ojima H. 1993. Dendritic arborization patterns of cortical interneurons labeled with the lectin, *Vicia villosa*, and injected intracellularly with Lucifer yellow in aldehyde-fixed rat slices. J Chem Neuroanat. 6:311–321.

Otsuka T, Kawaguchi Y. 2011. Cell diversity and connection specificity between callosal projection neurons in the frontal cortex. J Neurosci. 31:3862–3870.

Otsuka T, Kawaguchi Y. 2008. Firing-pattern-dependent specificity of cortical excitatory feed-forward subnetworks. J Neurosci. 28:11186–11195.

Paxinos G, Watson C. 2007. The rat brain in stereotaxic coordinates. 6th ed. San Diego: Elsevier.

Peters A, Payne BR. 1993. Numerical relationships between geniculocortical afferents and pyramidal cell modules in cat primary visual cortex. Cereb Cortex. 3:69–78.

Richardson RJ, Blundon JA, Bayazitov IT, Zakharenko SS. 2009. Connectivity patterns revealed by mapping of active inputs on dendrites of thalamorecipient neurons in the auditory cortex. J Neurosci. 29:6406–6417.

Rubio-Garrido P, Pérez-De-Manzo F, Porrero C, Galazo MJ, Clascá F. 2009. Thalamic input to distal apical dendrites in neocortical layer 1 is massive and highly convergent. Cereb Cortex. 19:2380–2395.

Schoonover CE, Tapia JC, Schilling VC, Wimmer V, Blazeski R, Zhang W, Mason CA, Bruno RM. 2014. Comparative strength and dendritic organization of thalamocortical and corticocortical synapses onto excitatory layer 4 neurons. J Neurosci. 34:6746–6758.

Stepanyants A1, Tamás G, Chklovskii DB. 2004. Class-specific features of neuronal wiring. Neuron 43:251–259.

Strick PL, Dum RP, Fiez JA. 2009. Cerebellum and nonmotor function. Annu Rev Neurosci. 32:413–434.

Uematsu M, Hirai Y, Karube F, Ebihara S, Kato M, Abe K, Obata K, Yoshida S, Hirabayashi M, Yanagawa Y, et al. 2008. Quantitative chemical composition of cortical GABAergic neurons revealed in transgenic Venus-expressing rats. Cereb Cortex. 18:315–330.

Ueta Y, Hirai Y, Otsuka T, Kawaguchi Y. 2013. Direction- and distance-dependent interareal connectivity of pyramidal cell subpopulations in the rat frontal cortex. Front Neural Circuits. 7:164.

Ueta Y, Otsuka T, Morishima M, Ushimaru M, Kawaguchi Y. 2014. Multiple layer 5 pyramidal cell subtypes relay cortical feedback from secondary to primary motor areas in rats. Cereb Cortex. 24:2362–2376.

Uhlhaas PJ, Singer W. 2012. Neuronal dynamics and neuropsychiatric disorders: toward a translational paradigm for dysfunctional large-scale networks. Neuron. 75:963–980.

Ushimaru M, Ueta Y, Kawaguchi Y. 2012. Differentiated participation of thalamocortical subnetworks in slow/spindle waves and desynchronization. J Neurosci. 32:1730–1746.

White EL, Rock MP. 1980. Three-dimensional aspects and synaptic relationships of a Golgi-impregnated spiny stellate cell reconstructed from serial thin sections. J Neurocytol. 9:615–636.

Wilke SA, Antonios JK, Bushong EA, Badkoobehi A, Malek E, Hwang M, Terada M, Ellisman MH, Ghosh A. 2013. Deconstructing complexity: serial block-face electron microscopic analysis of the hippocampal mossy fiber synapse. J Neurosci. 33:507-522.

Yuste R, Bonhoeffer T. 2004. Genesis of dendritic spines: insights from ultrastructural and imaging studies. Nat Rev Neurosci. 5:24–34.